Journal of Geophysical Research: Solid Earth

Supporting Information for

Mechanical implications of creep and partial coupling on the world's fastest slipping low-angle normal fault in southeastern Papua New Guinea

James Biemiller[1], Carolyn Boulton[2], Laura Wallace[1,3], Susan Ellis[3], Timothy Little[2], Marcel Mizera[2,4], Andre Niemeijer[4], Luc Lavier[1]

[1] Institute for Geophysics, Jackson School of Geosciences, University of Texas at Austin, Austin, Texas, USA.
[2] School of Geography, Environment and Earth Sciences, Victoria University of Wellington, Wellington, New Zealand.
[3] GNS Science, Lower Hutt, New Zealand.
[4] Faculty of Geosciences, Utrecht University, Utrecht, The Netherlands.

Contents of this file

Text S1 to S6
Figures S1 to S7
Tables S1 to S7

Additional Supporting Information

Dataset S1

Introduction

The Supporting Information text further details GPS analysis and experimental friction methods, models, and supplementary results. Figures illustrate additional GPS modeling results, and provides a more detailed map with locations of samples tested in friction experiments. Tables provide GPS positions and velocities, GPS modeling inputs and results, fault rock sample descriptions and friction experiment results. Dataset S1 gives experimental friction laboratory results (see Text S6 for details).

Text S1. GPS uncertainty calculations

Formal uncertainties for GPS velocities, particularly from campaign observations, tend to underestimate their true uncertainty (e.g., Zhang et al., 1997; Williams et al., 2004). To correct for underestimated uncertainties, a random-walk noise component is commonly incorporated into the final uncertainties. This correction scales with the inverse of the square root of the observation period, given in Zhang et al. (1997) as:

$$\sigma_{RWN} = \frac{A_{RWN}}{\sqrt{T}} \quad \text{(S1)}$$

where T is the time series duration and A_{RWN} is the amplitude of the random walk noise. Following Koulali et al. (2015)'s study of Papua New Guinea GPS velocities, we use random walk noise increments of 0.3 mm/$\sqrt{\text{yr}}$ for continuous sites and 1.0 mm/$\sqrt{\text{yr}}$ for campaign sites. Formal and corrected uncertainties are shown in Table S2 columns 8-11.

Text S2. Earthquake offset corrections

Static elastic coseismic displacements due to far-field (~100 – 1,000 km) large earthquakes range from < 1 mm to 10's of mm (e.g., Banerjee et al., 2005; Tregoning et al., 2013) depending on the distance from the hypocenter, the regional crustal elastic stratification, the spatial distribution of slip, and slip characteristics such as rake and total slip (Pollitz et al., 1996). Tregoning et al. (2013) showed that M_w >8.0 earthquakes caused mm-scale offsets within ~1000 km of their epicenters. Correcting for such offsets is especially important in studies where the velocity signal of interest is small (mm-scale), as is the case for velocities across the Mai'iu fault. Therefore, we calculate coseismic corrections for all $M_w \geq 6.9$ (based on USGS catalogue magnitudes) earthquakes with hypocentral depths < 100 km located within 700 km of our Mai'iu fault network (Fig. 1) from 2008 to June 2018.

We use a spherical layered Earth model (Pollitz, 1996) of harmonic degree 1 to 1500 with PREM elastic stratification (Dziewonski & Anderson, 1981) to calculate surface displacements at our GPS sites due to uniform slip on prescribed fault source models. For the 2016 Mw 7.9 Solomon Islands earthquake (~725 km from our network), we use two fault planes to approximate the composite megathrust source model of Lee et al. (2018), which matches observed teleseismic waveforms better than other proposed source models. This source model ascribes all coseismic slip to patches of the curved subduction megathrust and hence predicts larger horizontal displacements at our GPS sites than source models with rupture of an intraslab fault (Lay et al., 2017; USGS finite fault model). We find that surface displacements predicted by the model of Lee et al. (2018) best match those estimated from time-series analysis of continuous GPS data from site PNGM, the nearest continuous GPS site with similar azimuth to the hypocenter as our sites.

For other nearby 2008-2018 $M_w \geq 6.9$ earthquakes (~350 – 825 km from our network), we approximate the USGS finite fault models (Hayes, 2017; U.S. Geological Survey, 2019) as finite planes with uniform slip. For the few events without published finite fault models, we estimate slip planes based on hypocentral depth, focal mechanism solutions, regional tectonics and nearby event characteristics constrained by typical subduction zone earthquake length-width ratios from Strasser et al. (2010), as most of these events were subduction thrust events near the New Britain and San Cristobal trenches. The earthquake closest to our network was the 2010 M 6.9 New Britain event (~350 km away), while the earthquake with the largest static coseismic offsets at our sites was the 2016 M 7.9 New Britain event (~700 km away). We also reevaluate and correct for coseismic offsets due to the 2 April 2007 M_w 8.1 Solomon Islands earthquake using the coseismic slip model of Wallace et al. (2015), which was developed by jointly inverting horizontal GPS displacements and vertical displacements from coral paleogeodetic observations in the Solomon Islands (Taylor et al., 2008) (Fig. S2). All slip

models are tuned to approximately match the seismologically inferred M_w using a shear modulus of 25 GPa, and the details of each are listed in Table S3. GPS positions are corrected by adding static offset corrections equal and opposite to the modeled coseismic offsets during the GLOBK stage of processing.

Text S3. Block modeling (TDEFNODE)

Using the preferred block and fault configuration (Figures 2a, S3; Table S5), we perform inversions with different constraints on fault locking to explore how model constraints influence preferred locking distributions and data misfits. For example, the best-fit model (Figure 2) results from inversions where the coupling ratio (Φ) is required to decrease with increasing depth for all faults. We also test models where Φ is free to increase or decrease with depth (Figure S4a), as well as models where the Mai'iu fault is prescribed to be fully creeping (Φ = 0) or fully locked (Φ = 1) at all depths (Figures S4b, S4c, respectively), or fully locked at the surface (Figure S4d) or from the surface to 2, 4, 9, or 14 km depth (Figures S4e, S4f, S4g, S4h, respectively).

Text S4. Dislocation modeling of vertical velocities

Vertical velocities can also be valuable for investigating fault locking processes (e.g., Segall, 2010). However, because horizontal displacements are larger than vertical displacements for LANFs and vertical GPS uncertainties are typically 3–5 times larger than horizontal ones (e.g., Bennett et al., 2007; Serpelloni et al., 2013), we first consider only the strike-perpendicular horizontal velocities. Vertical velocities also suffer from an indeterminate reference frame problem and can be influenced by regional-scale uplift or subsidence processes unrelated to fault slip. Horizontal velocities can be tied to the rigid block motion of adjacent crustal blocks to isolate the components related to fault slip or locking. To address these issues, some authors select the site least likely to be affected by vertical tectonic motions and use its vertical velocity as the vertical reference frame (e.g., Beavan et al., 2010). Even with this method and high-precision continuous GPS observations, it is necessary to arbitrarily adjust all velocities by a baseline value in order to compare them to analytical physical models of crustal deformation (Beavan et al., 2010).

Vertical velocities across the fault show a sharp change on the order of 5 mm/yr from subtle footwall subsidence to hanging wall uplift near the fault trace, decaying to hanging wall subsidence with distance from the trace. At face value, the wavelength of vertical velocity change across the hanging wall suggests deeper locking than the horizontal velocities alone. Including both horizontal and vertical velocities, the best-fit ($\chi^2 = 2.41$) model fault dips 32° and slips at 13.5 mm/yr below a locking depth of 13 km. However, addressing the vertical reference frame ambiguity by allowing for a uniform modeled vertical velocity shifts across all sites of -5 to +5 mm/yr leads to a best-fit ($\chi^2 = 1.53$) model fault dipping 28° and slipping 10 mm/yr below a locking depth of 3 km, similar to the best-fitting model from horizontal velocities alone, with -3 mm/yr uniform vertical velocity shift.

Text S5. Quantitative X-ray diffraction methods

Eight fault rock samples (Table S4) were analyzed by X-Ray Diffraction by Mark Raven at CSIRO Land and Water Flagship, Mineral Resources Flagship, at the Centre for Australian Forensic Soil Science (CAFSS), in Urrbrae, South Australia. From these samples, 1.5 g sub-samples were ground for 10 minutes in a McCrone micronizing mill under ethanol. The resulting slurries were

oven dried at 60 °C then thoroughly mixed in an agate mortar and pestle before being lightly pressed into aluminum sample holders for X-ray diffraction analysis. XRD patterns from the micronized materials showed variable hydration of the interlayer which causes problems with quantification. Because the samples did not appear to contain any water-soluble phases, they were calcium saturated, and the data were re-analyzed. XRD patterns were recorded with a PANalytical X'Pert Pro Multi-purpose Diffractometer using Fe filtered Co Ka radiation, auto divergence slit, 2° anti-scatter slit and fast X'Celerator Si strip detector. The diffraction patterns were recorded in steps of 0.016° 2θ with a 0.4 second counting time per step, and logged to data files for analysis. XPLOT and HighScore Plus (PANalytical) search and match software were used to perform qualitative analysis. The abundance of identified mineral phases was then determined using SIROQUANT software from Sietronics Pty Ltd. Results are normalized to 100% and do not include unidentified or amorphous phases. Table S4 lists each sample's mineral phases and their relative proportion.

Text S6. Hydrothermal Friction Experiments

Complete hydrothermal friction results can be found in Supplementary Dataset S1. The text file contains data in tab delimited columns arranged by experiment (see Table S7 for experiment details). Lower case "d" denotes displacement (mm) and μ denotes the corrected coefficient of friction. Acquired raw torque and normal force data were processed to obtain shear stress and normal stress measurements respectively. Raw, externally measured, torque data were corrected for fluid pressure and shear displacement-dependent friction of the Teflon-coated O-ring seals using calibration values obtained in runs with a dummy sample of carbon-coated PolyEtherEtherKeton with a known sliding friction; seal friction is typically around 0.03 kN (equivalent to ~1.5 MPa shear stress). The contribution of the Molykote-coated confining rings to the measured friction is negligible (see also den Hartog et al., 2012a). The applied normal stress was corrected for the stress supported by the internal seals, the level of which is clearly visible during initial loading and was generally around 0.5 kN (equivalent to ~2 MPa normal stress acting on the sample).

In general, most fault gouges strengthen with increasing simulated depth (i.e. increasing temperature, effective normal stress, and fluid pressure) during an individual experiment. In some experiments, strengthening is the result of a long-term displacement-dependent increase in friction (e.g. Figure 5c), whereas in other experiments strengthening is abrupt and is the result of increased simulated depth (e.g. Figure 5b). The repeat experiment pairs u368+u370, u369+u371 and u546+u547 (note that a different velocity profile was applied in experiments u368 and u369) show good reproducibility in terms of the general evolution of friction with displacement, the level of friction and the velocity dependence of friction. Variability in friction is less than 0.05 in all cases and less than 0.02 in most cases. Unstable sliding (stick-slips) is encountered in only a few experiments, typically at a temperature range between 250 °C and 350 °C at low sliding velocity (< 30 μm/s) for samples with a friction coefficient of at least 0.6 (Figures 5b,d). Some history dependence (i.e. displacement dependence) is seen in the experiments performed at the highest temperatures (i.e., 300-350-400-450 °C), in which the first series of velocity steps reproduces the temperature conditions of the last series of velocity steps performed in the low temperature experiment (Table S7). The friction coefficient recorded at low displacements at 300°C is consistently lower than that recorded at high displacements at 300 °C, except for experiment u775. It should be noted that both effective normal stress and fluid pressure are considerably lower in the low-displacement 300 °C steps (120 vs. 180 MPa and 80 vs. 180 MPa, respectively), which might explain the difference.

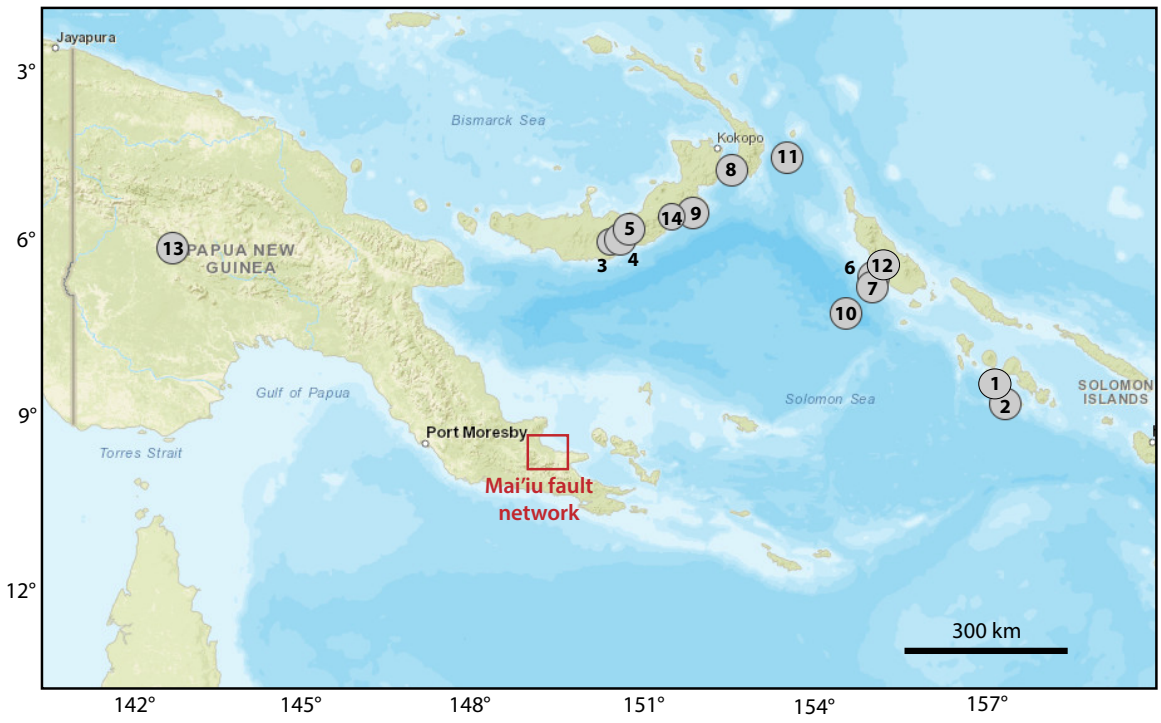

Figure S1. Regional earthquakes of M ≥ 6.9 corrected for using STATIC1D (Text S2; U.S. Geological Survey, 2019). See Table S2 and Text S2 for a list and description of these events. Labeled numbers refer to event numbers in Table S2.

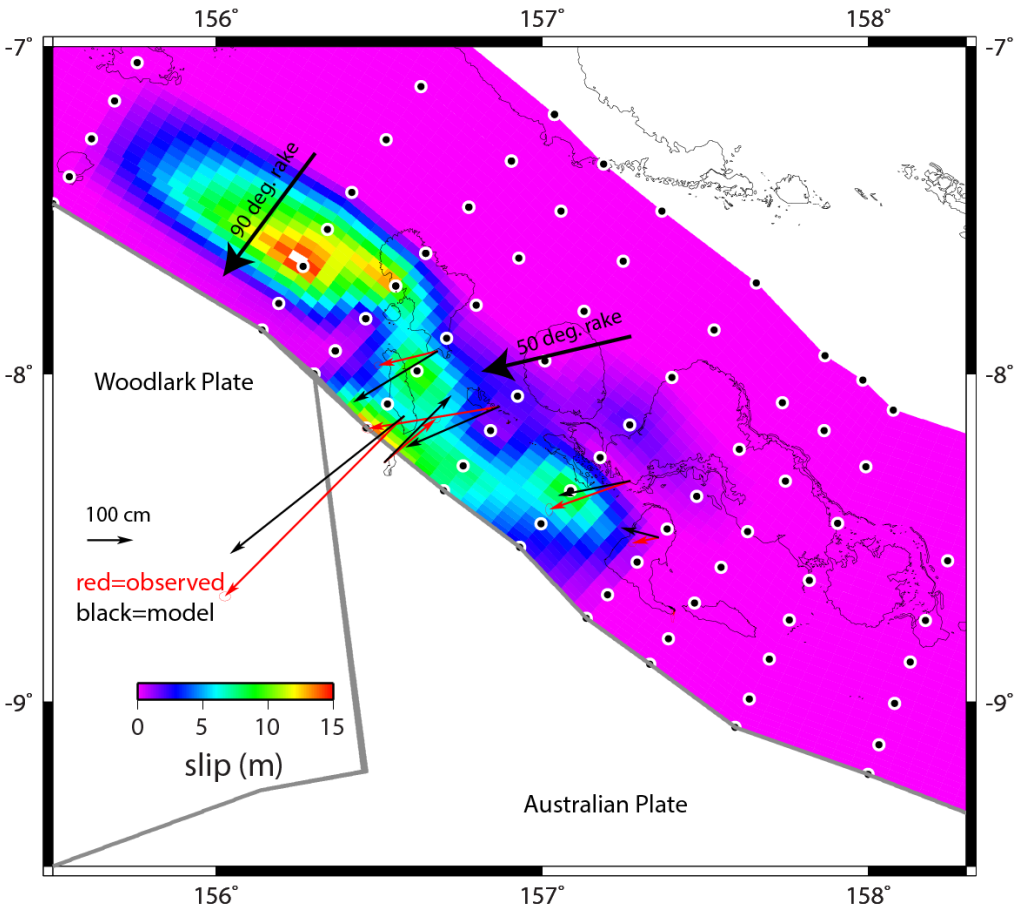

Figure S2. Slip distribution for the 2007 M 8.1 Solomon Islands earthquakes from joint inversion of campaign GPS displacements (red vectors) and coastal uplift/subsidence recorded by coral reef platforms (Wallace et al., 2015). Black vectors show the modeled fit to the horizontal component of GPS velocities. Larger black vectors show the rake of slip.

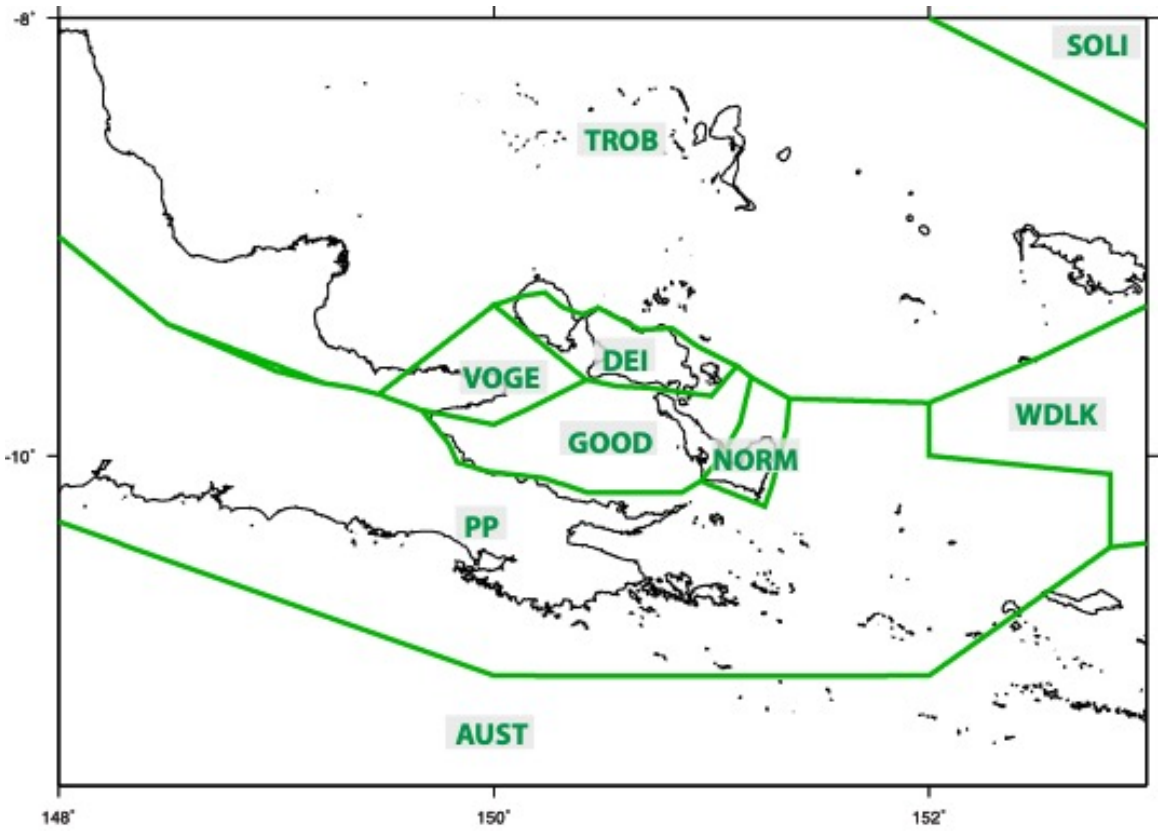

Figure S3. Individual blocks tested for independence. *F* tests cannot statistically distinguish between models where VOGE and GOOD are considered individual blocks and ones where they are one unified block (Table S5). Therefore, we treat them as one block in subsequent TDEFNODE block models (configuration 2 in Table S5). TROB = Trobriand Islands block; SOLI = Solomon Islands block; WDLK = Woodlark Plate block; DEI = D'Entrecasteaux Islands block (Goodenough & Fergusson Islands); NORM = Normanby Island block; VOGE = Cape Vogel block; GOOD = Goodenough Basin block; PP = Papuan Peninsula block; AUST = Australian Plate block.

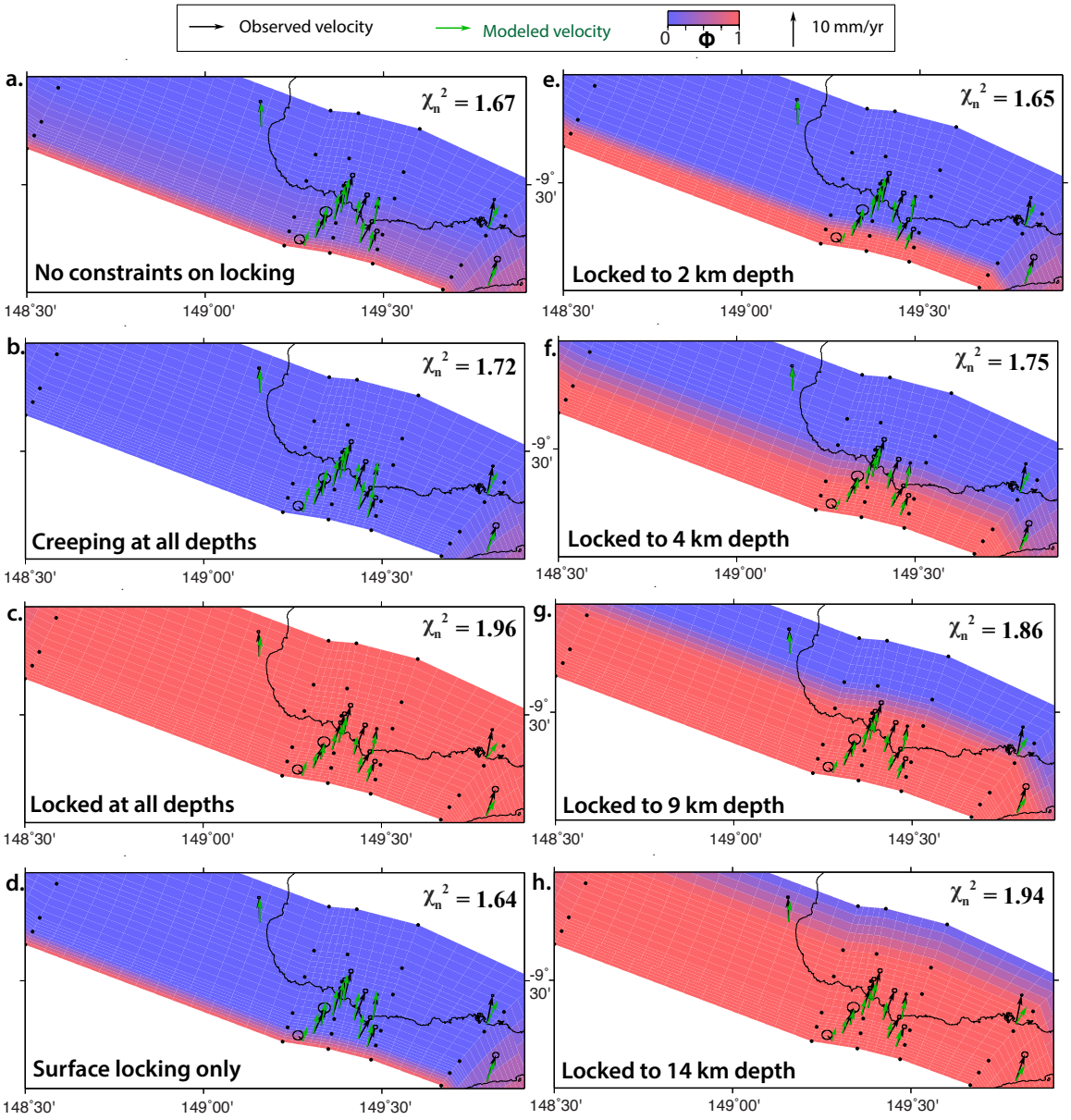

Figure S4. Mai'iu fault locking results for different inversion constraints and locking depths in the elastic block models. We test models where the kinematic coupling ratio, Φ, is free to increase or decrease with depth (a), as well as models where the Mai'iu fault is prescribed to be fully creeping (Φ = 0) or fully locked (Φ = 1) at all depths (b, c, respectively), or fully locked at the surface (d) or from the surface to 2, 4, 9, or 14 km depth (e, f, g, h, respectively).

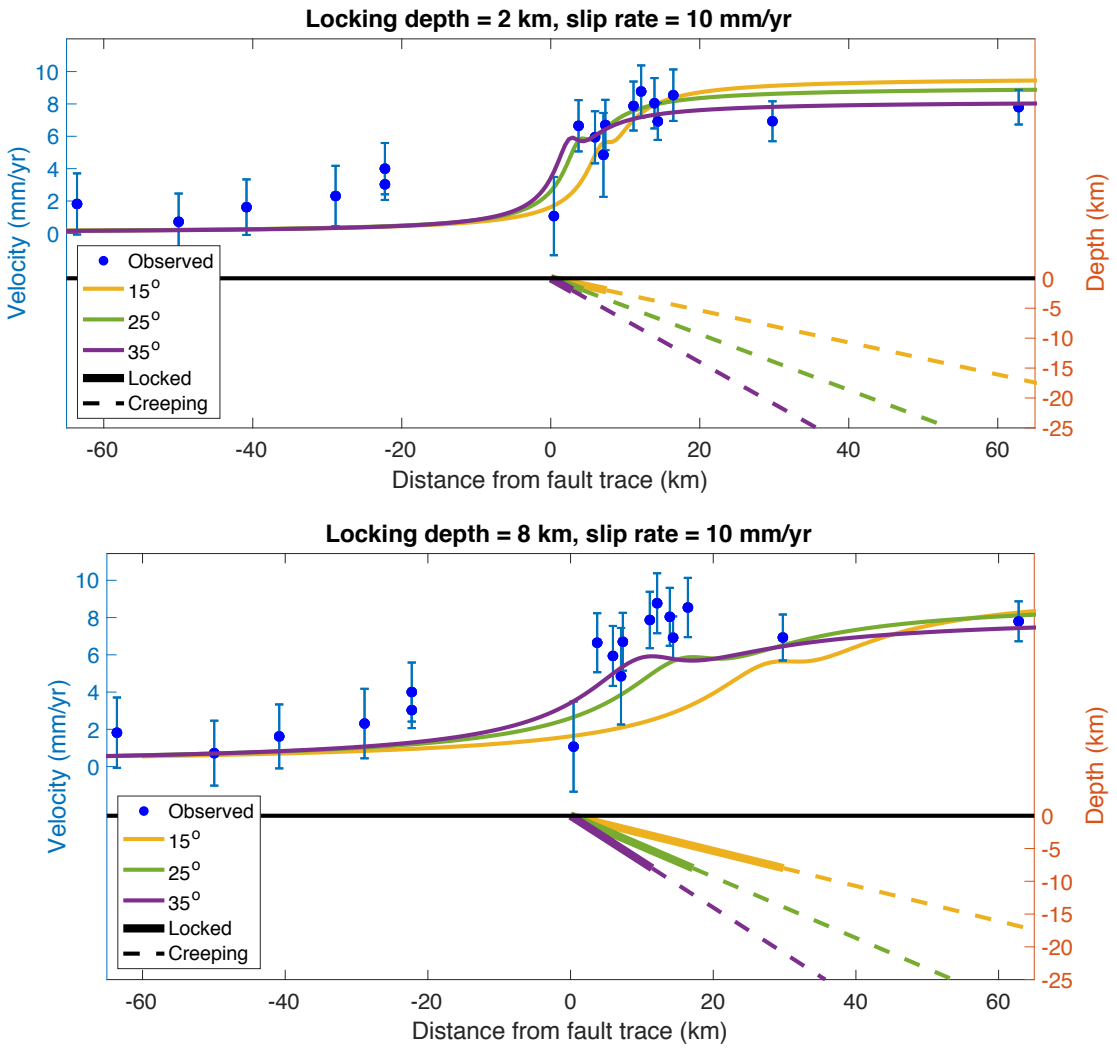

Figure S5. Illustrated example of tradeoffs between locking depth, fault dip and predicted velocities for planar dislocation models with locking at the surface. Observed velocities are parallel to profile X-X′ of Fig. 2a and are relative to a fixed Australian plate. Fault dip has less effect on velocities for shallowly locked faults than for more deeply locked faults.

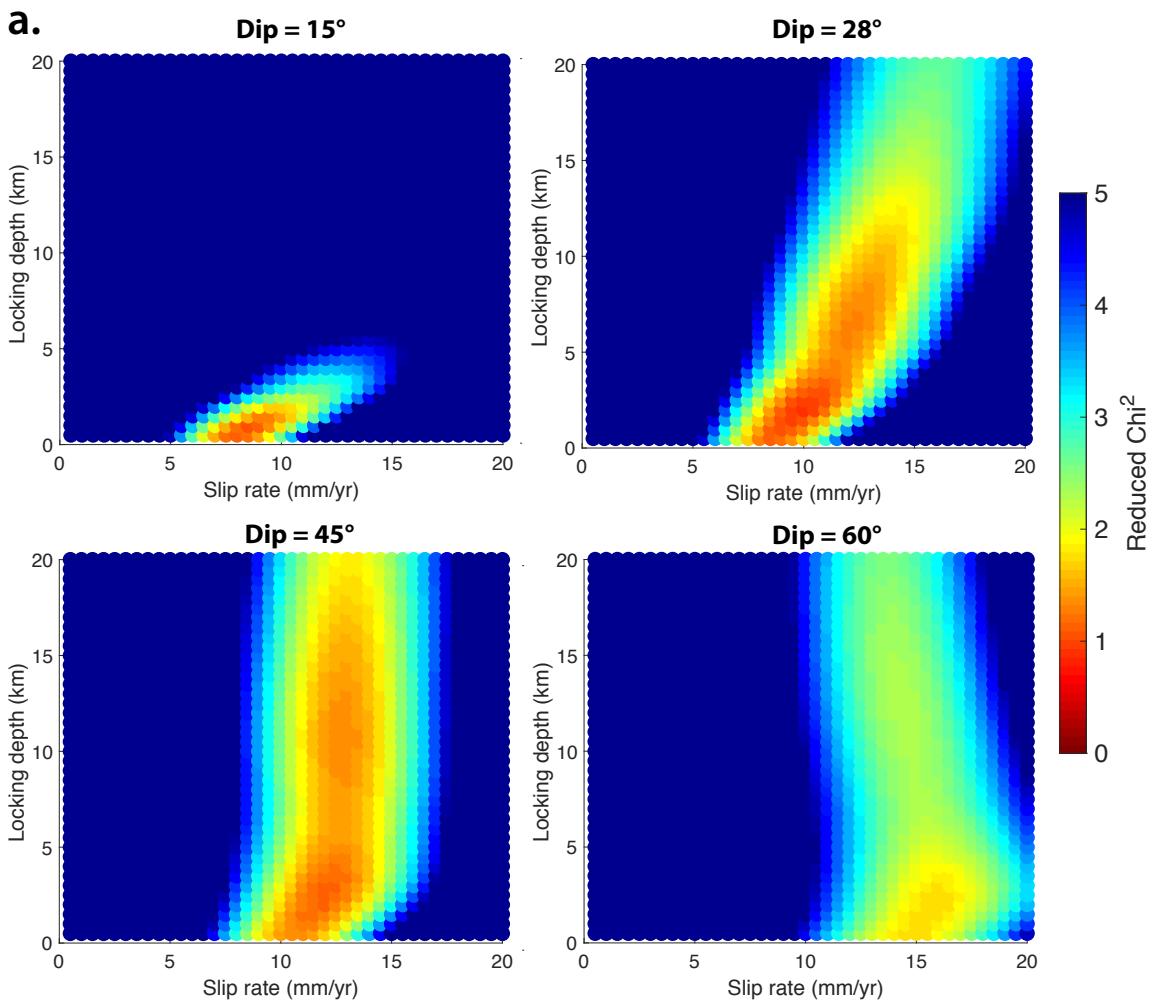
a.
Dip = 15°
Dip = 28°
Dip = 45°
Dip = 60°
Locking depth (km)
Slip rate (mm/yr)
0
5
10
15
20
Reduced Chi2
0
1
2
3
4
5

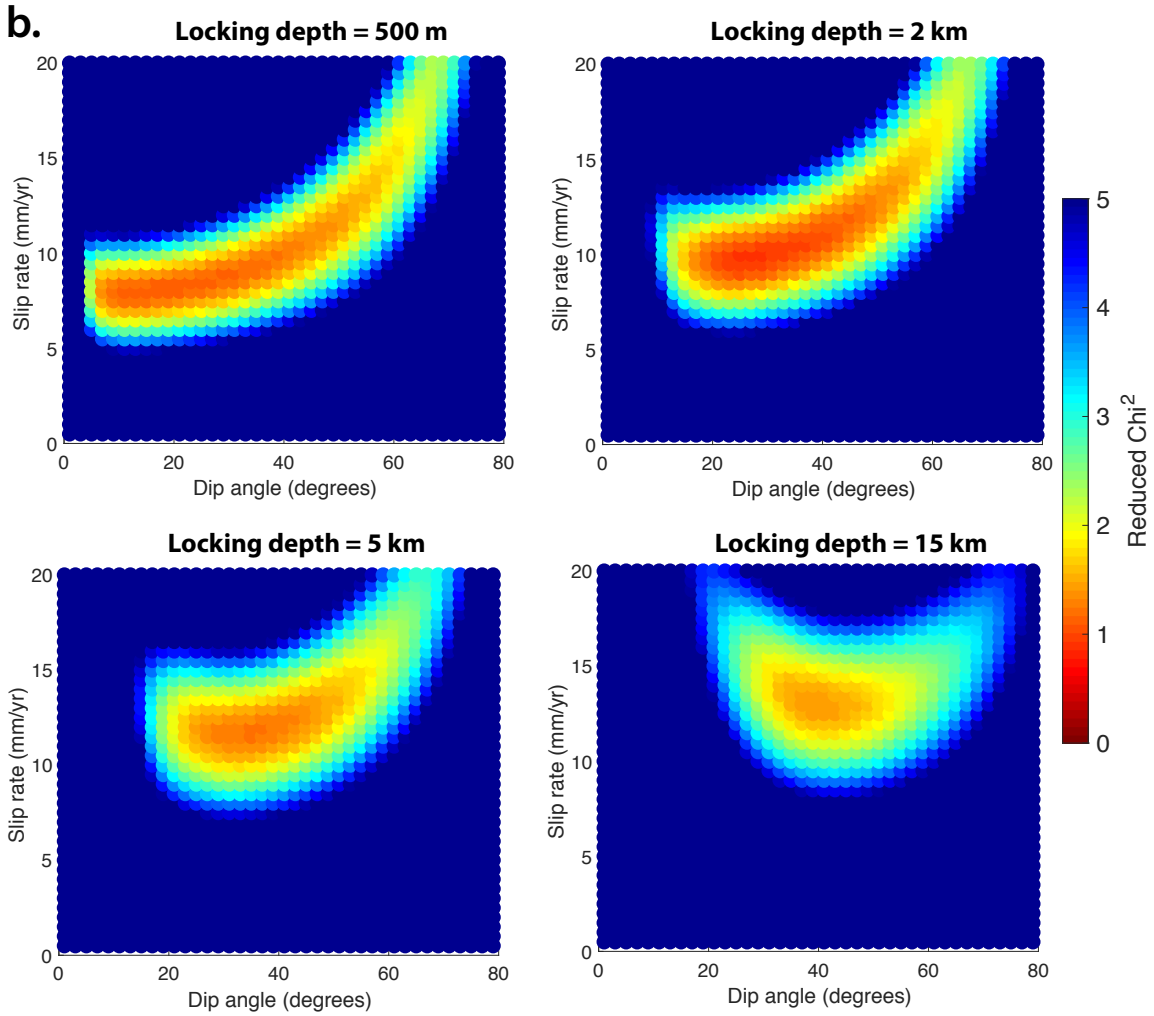
b.
Locking depth = 500 m
Locking depth = 2 km
Locking depth = 5 km
Locking depth = 15 km
Slip rate (mm/yr)
Dip angle (degrees)
Reduced Chi2
0
5
10
15
20
0
20
40
60
80
0
1
2
3
4
5

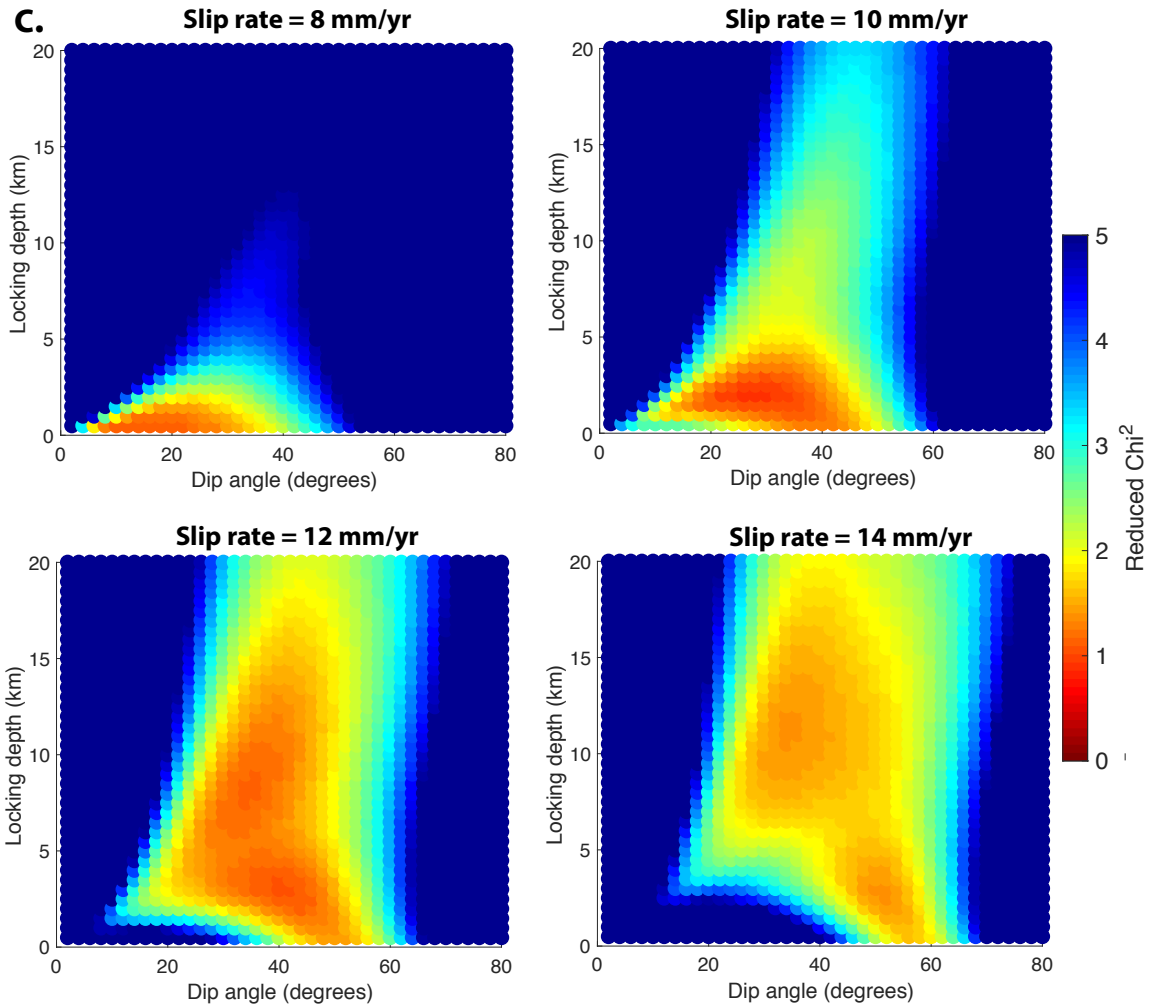

Figure S6. Parameter sensitivity plots for locked-to-surface dislocation models showing data misfit (reduced χ^2) tradeoffs between: a.) slip rate and locking depth for dips of 15°, 28°, 45°, and 60°; b.) dip angle and slip rate for locking depths of 0.5, 2, 5, and 15 km; c.) dip angle and locking depth for slip rates of 8, 10, 12, and 14 mm/yr.

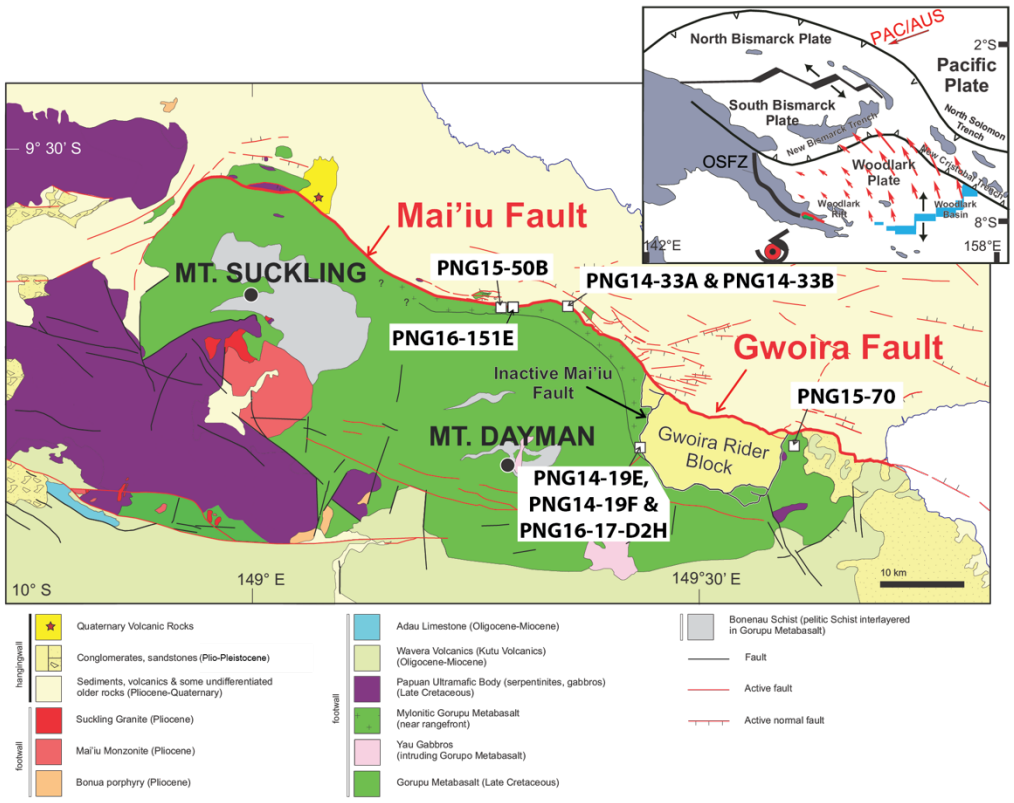

Figure S7. Tectonic setting (inset) and geological map showing the active and inactive strands of the Mai'iu Fault and the location of the fault rocks analyzed. Each fault rock is identified by its field sample number. Map after Little et al. (2019) and Mizera et al (2020).

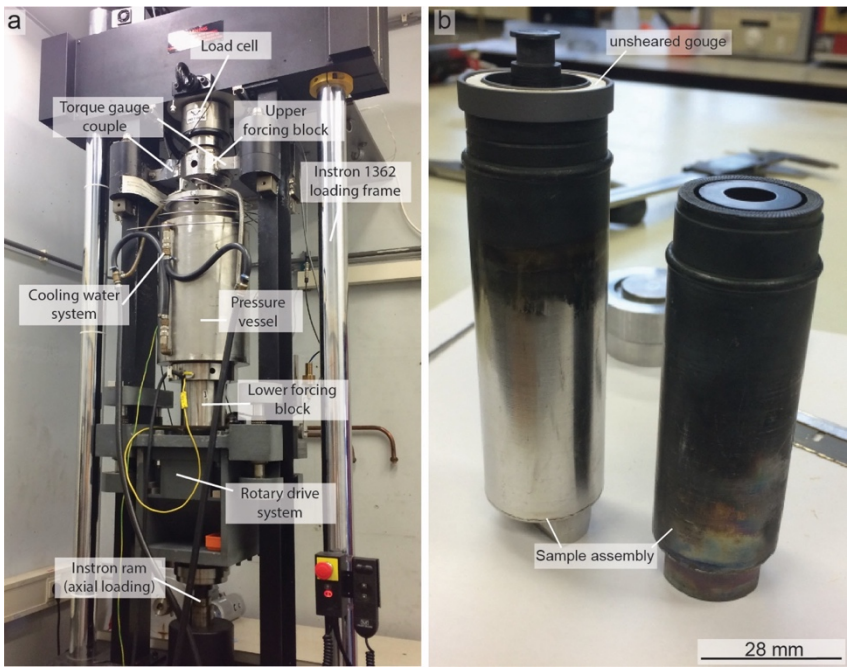

Figure S8. Images of the High Temperature and Pressure (HPT) Lab, Utrecht University, hydrothermal ring shear apparatus used to measure the frictional properties of Mai'iu fault rock samples. (a) is a labelled photograph of the apparatus, and (b) depicts the two pistons which, fitted together with an annulus of gouge between them, are inserted into the pressure vessel and sheared under controlled conditions of temperature, effective normal stress, and velocity.

Site	2002	2004	2005	2006	2008	2009	2010	2012	2015	2016	2018
AGAN									x		x
ALT2	x	x				x	x	x			
BASM						x	x	x			
BAYA						x	x	x	x		
BINI									x	x	x
BORO									x	x	x
BWAR						x	x	x			
DAIO						x	x	x			
DARB						x	x	x			
DD01									x	x	
DIGA						x	x	x			
ESAA		x			x		x	x			
GIWA						x	x	x			
GONO									x	x	x
GOUR									x	x	x
GUA1		x					x				
GUMA						x	x	x			
HEHE						x	x	x			
JONE						x	x	x			
KABU									x	x	
KALO						x	x	x			x
KAWA						x	x	x			
KEIA						x	x	x			
KIBU									x	x	x
KILI						x	x	x			x
KURA						x	x	x			
KWAN						x	x	x			
KWAT						x	x	x			
LELE						x	x	x			
LOS2		x					x	x			
MAAP						x	x	x			
MENA						x	x	x			
MORA						x	x	x			x
MORB									x	x	x
NUBE						x	x	x			
PEMM						x	x	x		x	
RAB2							x				x
RABA						x	x	x			x

RAKO									x	x	x
SALM		x				x	x	x			
SIBA						x	x	x			
SIRI						x	x	x			
SMRI						x	x	x			
STRA						x	x	x			
TUF2						x	x	x	x		x
TUFI		x	x	x							
UAMA						x	x	x			
VAKU						x	x	x			
VIVI					x		x				
WAIB						x	x	x			x
WANI						x	x	x		x	
WAPO						x	x	x			
WATL		x			x		x	x			
YAMS									x	x	
YANA						x	x	x			

Table S1. GPS sites and observation years used in this study.

Site	Longitude	Latitude	V_N^{IT14}	V_E^{IT14}	V_N^{AUS}	V_E^{AUS}	σ_N^f	σ_E^f	σ_N^{rwn}	σ_E^{rwn}
	°	°	mm/yr	mm/yr	mm/yr	mm/yr	mm/yr	mm/yr	mm/yr	mm/yr
AGAN	149.387	-9.93	34.21	59.4	3.90	1.01	0.63	0.74	1.20	1.31
ALT2	150.338	-10.31	35.05	57.54	2.41	2.20	0.14	0.16	0.45	0.47
BASM	150.833	-9.466	34.85	68.54	13.60	1.66	0.76	0.87	1.33	1.44
BAYA	149.474	-9.608	34.6	62.4	6.93	1.26	0.23	0.27	0.63	0.67
BINI	149.308	-9.648	36.19	61.57	6.04	2.84	0.61	0.73	1.20	1.32
BORO	149.459	-9.684	35.57	60.97	5.50	2.27	0.64	0.78	1.23	1.37
BWAR	151.185	-9.94	36.04	58.13	3.34	3.15	0.88	1.00	1.46	1.58
DAIO	150.427	-10.408	34.12	57.06	1.96	1.34	1.08	1.25	1.65	1.82
DARB	151.015	-9.927	33.86	57.98	3.12	0.93	0.97	1.06	1.55	1.64
DD01	149.289	-9.835	35.91	54.54	-1.00	2.65	1.60	1.88	2.57	2.85
DIGA	151.204	-10.2	34.67	58.42	3.63	1.91	1.53	1.55	2.11	2.13
ESAA	150.812	-9.739	37.41	59.87	4.93	4.35	0.34	0.42	0.70	0.78
GIWA	149.794	-9.78	35.74	62.69	7.35	2.54	1.12	1.33	1.70	1.91
GONO	149.434	-9.661	36.73	61.35	5.87	3.41	0.56	0.68	1.15	1.27
GOUR	149.362	-9.597	35.69	63.05	7.54	2.33	0.51	0.61	1.10	1.20
GUA1	152.944	-9.225	36.57	83.52	29.47	3.58	0.37	0.45	0.77	0.85
GUMA	150.865	-9.21	32.55	70.84	15.92	-0.76	0.80	0.93	1.38	1.51
HEHE	150.874	-10.226	34.28	58.02	3.10	1.48	1.07	1.27	1.65	1.85
JONE	150.102	-10.095	34.97	58.02	2.79	1.97	0.77	0.87	1.34	1.44
KABU	149.33	-9.624	34.24	60.38	4.86	0.89	2.05	2.64	3.07	3.66
KALO	150.43	-9.414	34.54	63.94	8.84	1.26	0.22	0.24	0.55	0.57
KAWA	150.299	-8.522	26.69	69.17	14.02	-7.05	0.96	1.07	1.53	1.64
KEIA	150.554	-10.213	34.66	57.22	2.17	1.80	0.83	0.93	1.40	1.50
KIBU	149.381	-9.577	34.9	63.53	8.03	1.53	0.57	0.68	1.16	1.27
KILI	150.292	-9.496	34.91	63.94	8.79	1.65	0.23	0.26	0.56	0.59
KURA	151.036	-10.11	34.59	56.13	1.28	1.76	1.10	1.09	1.68	1.67
KWAN	151.274	-9.923	33.01	58.92	4.16	0.12	0.88	1.05	1.46	1.63
KWAT	150.712	-9.311	32.68	70.48	15.50	-0.61	0.72	0.80	1.30	1.38
LELE	150.728	-10.302	33.53	55.36	0.38	0.75	0.93	1.04	1.50	1.61
LOS2	151.125	-8.535	28.31	72.08	17.26	-5.30	0.25	0.31	0.61	0.67
MAAP	150.4374	-9.6104	35.55	62.5	7.41	2.37	0.39	1.12	1.18	1.70
MENA	149.936	-9.757	34.91	62.25	6.96	1.72	1.01	1.13	1.59	1.71
MORA	150.187	-9.432	33.51	64.14	8.95	0.20	0.22	0.24	0.55	0.57
MORB	149.422	-9.61	36.56	63.65	8.16	3.21	0.63	0.79	1.22	1.38
NUBE	149.867	-10.399	33.91	55.7	0.38	1.03	0.90	0.99	1.47	1.56
PEMM	149.795	-9.621	34.84	63.35	8.01	1.56	0.27	0.32	0.65	0.70
RABA	149.834	-9.972	35.44	58.79	3.46	2.34	0.10	0.12	0.37	0.39
RAKO	149.393	-9.557	35.43	63.86	8.36	2.05	0.61	0.75	1.20	1.34

SALM	150.796	-9.663	37.72	65.59	10.64	4.62	0.21	0.24	0.57	0.60
SIBA	150.268	-10.684	32.83	57.05	1.89	0.16	1.24	1.18	1.81	1.75
SIRI	149.708	-9.841	36.52	58.04	2.66	3.33	1.34	1.42	1.92	2.00
SMRI	150.662	-10.613	32.96	56.62	1.62	0.32	0.87	0.93	1.44	1.50
STRA	151.868	-10.225	34.72	58.69	4.18	2.09	0.82	0.90	1.40	1.48
TUF2	149.318	-9.079	32.1	63.18	7.65	-1.52	0.23	0.25	0.56	0.58
TUFI	149.323	-9.08	30.51	63.96	8.44	-3.10	0.95	1.09	1.65	1.79
UAMA	150.953	-9.452	33.38	70.92	16.03	0.20	1.16	1.35	1.73	1.92
VAKU	151.184	-8.853	30.03	72.51	17.72	-3.42	0.66	0.73	1.23	1.30
VIVI	150.324	-9.31	33.28	64.98	9.84	-0.07	0.97	1.12	1.68	1.83
WAIB	150.139	-9.245	33.73	66.61	11.40	0.32	0.24	0.26	0.57	0.59
WANI	149.157	-9.338	33.34	62.52	6.93	-0.18	0.35	0.42	0.73	0.80
WAPO	150.532	-9.355	32.76	69.06	14.00	-0.53	1.12	1.31	1.70	1.89
WATL	150.243	-9.211	32.89	66.21	11.04	-0.52	0.35	0.43	0.71	0.79
YAMS	149.279	-9.7	31.93	57.23	1.69	-1.41	2.18	2.50	2.77	3.09
YANA	151.897	-9.271	33.51	74.89	20.39	0.38	1.00	1.20	1.59	1.79

Table S2. Coordinates, velocities, and uncertainties for each GPS site. $\mathbf{V_N^{IT14}}$ and $\mathbf{V_E^{IT14}}$ are the North and East components of velocity in the ITRF14 reference frame. $\mathbf{V_N^{AUS}}$ and $\mathbf{V_E^{AUS}}$ are the North and East components of velocity relative to the Australian Plate. $\boldsymbol{\sigma_N^f}$ and $\boldsymbol{\sigma_E^f}$ are the formal uncertainties for the North and East velocity components. $\boldsymbol{\sigma_N^{rwn}}$ and $\boldsymbol{\sigma_E^{rwn}}$ are the uncertainties of the North and East velocity components after correcting for random-walk noise (Text S1).

Plate	Longitude (°)	Latitude (°)	Rotation Rate (°/Myr)	Major Axis Uncertainty (Distance in °)	Minor Axis Uncertainty (Distance in °)	Orientation of Major Axis (° East of North)
WDLK	148.92	-10.97	2.81 ± 0.40	0.77	0.19	82
TROB	147.75	-9.33	2.67 ± 0.23	0.42	0.19	75
DEI	147.90	-8.95	2.04 ± 1.11	1.93	0.34	104
GOOD	175.79	-18.84	-0.16 ± 1.00	102.36	3.54	107
NORM	150.42	-9.70	1.64 ± 0.28	0.68	0.52	151
PP	149.23	-9.40	0.73 ± 0.28	0.91	0.6	128

Plate	Ω_x	Ω_y	Ω_z	σ_x	σ_y	σ_z	cov(x,y)	cov(x,z)	cov(y,z)
WDLK	-2.36	1.43	-0.54	0.35	0.18	0.07	-0.0646	0.0255	-0.0132
TROB	-2.23	1.41	-0.43	0.20	0.11	0.03	-0.021	0.0066	-0.0036
DEI	-1.71	1.07	-0.32	0.95	0.54	0.18	-0.5127	0.1745	-0.0998
GOOD	0.15	-0.01	0.05	0.96	0.55	0.19	-0.5264	0.1775	-0.102
NORM	-1.41	0.80	-0.28	0.24	0.14	0.05	-0.0329	0.0125	-0.0072
PP	-0.62	0.37	-0.12	0.24	0.14	0.05	-0.0331	0.0119	-0.0069

Table S3. Poles of rotation of crustal blocks relative to the Australian Plate. Cartesian coordinates are shown in the lower section. Ω_x, Ω_y, and Ω_z are the Cartesian angular velocity vector components; σ_x, σ_y, and σ_z are the uncertainties of the respective components. The final columns give the covariances of component pairs. WDLK = Woodlark Plate; TROB = Trobriand Block; DEI = D'Entrecasteaux Islands block; GOOD = Goodenough Bay block; NORM = Normanby Island block; PP = Papuan Peninsula block.

#	Year	Event name	d_h	Lat.	Lon.	d_1	d_2	Str.	Dip	L	Rake	Slip	dE	dN	D
			km	°	°	km	km	°	°	km	°	m	mm	mm	km
1	2007	M 8.1 Solomon Isl.	24*												
2	2010	M 7.1 Solomon Isl.	10	-8.67	157.30	5	15	326	15	45	94	0.8			
3	2010	M 6.9 New Britain 1	28	-6.37	150.35	25	45	185	50	45	75	0.6			
4	2010	M 7.3 New Britain	35	-6.00	150.20	25	35	257	24	70	102	1.2			
5	2010	M 7.0 New Britain	44	-5.70	150.65	16	40	240	31	60	60	0.25			
6	2014	M 7.1 Bougainville 1	61	-6.39	154.97	50	75	310	45	50	80	0.7			
7	2014	M 7.5 Bougainville	43	-6.36	154.90	15	45	315	33	49	95	1.5			
8	2015	M 7.5 New Britain 1	41*												
		Segment 1		-5.40	152.25	12	17	252	44	120	61	0.3			
		Segment 2		-5.19	152.91	17	28	252	33	120	90	0.8			
		Segment 3		-5.08	152.16	28	43	252	24	120	65	0.5			
		Segment 4		-4.80	152.64	43	57	252	13	40	90	0.3			
9	2015	M 7.5 New Britain 2	55	-5.38	151.71	26	56	244	29	70	65	1			
10	2015	M 7.1 Bougainville 2	10	-7.54	154.87	0	16	125	67.5	80	270	1.2			
11	2016	M 7.9 New Britain 1	95*										7.90	7.62	725
		Segment 1		-5.00	153.00	0	50	313	27.9	260	90	1			
		Segment 2		-4.50	153.50	50	100	313	65	100	90	1			
12	2017	M 7.9 Bougainville	135	-6.70	155.20	136	166	135	55	50	90	8	3.16	1.98	750
13	2018	M 7.5 Highlands	25	-5.80	142.20	1	30	308	33	100	90	1	0.02	0.03	825
14	2018	M 6.9 New Britain 2	35	-5.82	151.07	25	45	244	45	45	82	0.6	0.04	0.55	500

Table S4. Events and fault parameters used in regional earthquake corrections, based on USGS finite fault models (U.S. Geological Survey, 2019). Latitude and longitude are given for the lower corner of the fault farthest along the strike direction. d_h is the hypocentral depth. d_1 and d_2 are the upper and lower depths of the fault, respectively. Str is the fault strike. L is the along-strike length of the slipping fault and slip is the total slip. For the events from 2016-2018 (during our Mai'iu fault campaign experiment), D is the approximate distance from the earthquake to our GPS sites near the Mai'iu fault, dE is the average magnitude of the eastward offset at our campaign sites due to each event, and dN is the average magnitude of the northward offset at our campaign sites due to each event. Red events had no available USGS finite fault model as of publication. * = events with non-planar or multi-segment sources (Text S2). Individual fault segment parameters are listed below these events, except for the 2007 Solomon Islands earthquake, for which the modeled slip distribution from Wallace et al. (2015) is shown in Fig. S2.

Config.	Description	N_{data}	N_{params}	DOF	χ^2	*F* test probability	Is (1) better?
1	Best fit	255	46	209	1.65		
2	VOGE + GOOD	255	43	212	1.69	57	No
3	VOGE + DEI + GOOD	255	39	216	1.93	87	Probably
4	GOOD + NORM	255	42	213	2.02	93	Probably
5	GOOD + NORM + DEI	255	38	217	1.95	89	Probably
6	DEI + TROB	255	38	217	1.82	76	Probably

Table S5. Results of *F* test for block independence based on GPS velocities in Table S2 and block boundary configurations in Figure S3. N_{data} = number of data; N_{params} = number of free parameters; DOF = degrees of freedom. 'VOGE + DEI + GOOD' refers to models where Cape Vogel (VOGE), Goodenough Bay (GOOD), and D'Entrecasteaux Islands (DEI) blocks are treated as one unified block rotating about one pole. *F* tests cannot statistically distinguish between models where VOGE and GOOD are considered individual blocks (configuration 1) and ones where they are one unified block (configuration 2). Therefore, we treat them as one block in all TDEFNODE block models.

CSIRO ID	Field Sample #	Fault rock	Lat. (°S), Long (°E) (WGS84)	Quantitative mineralogy
42351	PNG14-19E	upper gouge	-9.82862, 149.44082	Corrensite/Saponite (65%), Augite (13%), Kaolin (8%), Amphibole (6%), Plagioclase (4%), Quartz (2%), Calcite (2%)
42352	PNG14-19F	lower gouge	-9.82862, 149.44082	Corrensite/Saponite (49%), Amphibole (18%), Augite (17%), Plagioclase (8%), Kaolin (4%), Quartz (1%), Calcite (3%)
42358	PNG14-33B	upper mafic gouge	-9.67726, 149.35904	Corrensite/Saponite (21%), Calcite (21%), Montmorillonite (11%), Plagioclase (11%), Epidote (9%), Kfeldspar (7%), Amphibole (5%), Quartz (5%), Chlorite (4%), Dolomite/Ankerite (3%), White mica (3%)
42357	PNG14-33A	lower mafic gouge	-9.67726, 149.35904	Plagioclase (30%), Epidote (18%), Amphibole (16%), Corrensite/Saponite (8%), Chlorite (7%), Titanite (6%), Stilpnomelane (6%), Quartz (3%), Calcite (3%), Kfeldspar (2%)
52980	PNG16-17-D2H	foliated cataclasite	-9.8297, 149.4403	Epidote (26%), Plagioclase (19%), Quartz (20%), Calcite (12%), Amphibole (9%), Corrensite/Saponite (8%), Chlorite (3%), Titanite (3%)
52979	PNG16-151E	foliated cataclasite	-9.6790, 149.2941	Amphibole (37%), Plagioclase (29%), Epidote (22%), Chlorite (5%), Titanite (3%), Calcite (2%), White mica (2%), Quartz (<1%)
45071	PNG15-70	serpentinite	-9.82863, 149.61246	Lizardite Serpentine (82%), Magnesite (12%), Saponite (4%), Maghemite (1%), Quartz (<1%), Calcite (<1%), Dolomite/Ankerite (<1%)
45070	PNG15-50B	ultracataclasite	-9.67778, 149.28669	Corrensite (25%), Kfeldspar (22%), Plagioclase (20%), Amphibole (16%), Augite (12%), Chlorite (2%), Calcite (2%), Quartz (1%)

Table S6. Description and quantitative mineralogy of fault rock samples.

Exp.	*Sample #*	σ_n^{eff} *(MPa)*	P_f *(MPa)*	*T (°C)*	μ_{ss}
u368*	PNG-14-19F	30-60-90-120	20-40-60-80	50-100-150-200	0.24-0.18-0.19-0.26
u369*	PNG-14-19E	30-60-90-120	20-40-60-80	50-100-150-200	0.14-0.11-0.13-0.13
u370	PNG-14-19F	30-60-90-120	20-40-60-80	50-100-150-200	0.23-0.21-0.20-0.28
u371	PNG-14-19E	30-60-90-120	20-40-60-80	50-100-150-200	0.15-0.13-0.11-0.14
u487	PNG-15-50B^	120-150	80-100	200-250	0.63-0.74
u493	PNG-15-50B	90-120-150-180	90-120-150-180	150-200-250-300	0.59-0.59-0.66-0.72
u495	PNG-15-70	90-120-150-180	90-120-150-180	150-200-250-300	0.37-0.41-0.48-0.57
u496	PNG-15-70	120-150-180-210	80-100-120-140	300-350-400-450	0.50-0.60-0.62-0.63
u497	PNG-15-50B	120-150-180-210	80-100-120-140	300-350-400-450	$0.75^{\#}$-0.80-0.80-0.73
u545	PNG-14-33B	30-60-90-120	20-40-60-80	50-100-150-200	0.22-0.26-0.28-0.35
u546	PNG-14-33A	30-60-90-120	20-40-60-80	50-100-150-200	0.41-0.46-0.50-0.56
u547	PNG-14-33A	30-60-90-120	20-40-60-80	50-100-150-200	0.40-0.44-0.48-0.57
u772	PNG-16-17D2H	90-120-150-180	60-80-100-120	150-200-250-300	0.75-0.72-0.73-$0.72^{\#}$
u773	PNG-16-151e	90-120-150-180	60-80-100-120	150-200-250-300	0.66-0.60-0.59-0.57
u774	PNG-16-17D2H	120-150-180-210	80-100-120-140	300-350-400-450	0.57-0.60-0.47-0.44
u775	PNG-16-151e	120-150-180-210	80-100-120-140	300-350-400-450	0.67-0.67-$0.66^{\#}$-0.61

Table S7. List of experiments performed with experimental conditions and values of friction (=shear stress / effective normal stress, ignoring cohesion) at the end of each run-in (at 1 mm/s). The sliding velocity was 1 mm/s initially and then stepped to 0.3-1-3-10-30 mm/s with 0.5-1.5-1.5-1.5-1.5 mm of displacement. Steady state friction (m_{ss}) is determined at the end of the run-in at 1 mm/s at each s_n^{eff}-T-P_f condition. * Run-in at 10 mm/s, step from 0.3 to 1 mm/s omitted, step from 30-100 mm/s included, ^ experiment terminated prematurely due to pore fluid leak, # indicates peak value of stick-slip.